SAE INTERNATIONAL®

An Extensive Validation of an Open Source Based Solution for Automobile External Aerodynamics

2017-01-1524
Published 03/28/2017

Robert Lietz, Levon Larson, Peter Bachant, John Goldstein, Rafael Silveira, and Mehrdad Shademan
Ford Motor Company

Pete Ireland and Kyle Mooney
ICON

CITATION: Lietz, R., Larson, L., Bachant, P., Goldstein, J. et al., "An Extensive Validation of an Open Source Based Solution for Automobile External Aerodynamics," SAE Technical Paper 2017-01-1524, 2017, doi:10.4271/2017-01-1524.

Copyright © 2017 SAE International

Abstract

The number of computational fluid dynamics (CFD) simulations performed during the vehicle aerodynamic development process continues to expand at a rapid rate. One key contributor to this trend is the number of analytically based designed experiments performed to support vehicle aerodynamic shape development. A second contributor is the number of aerodynamic optimization studies performed for vehicle exterior components such as mirrors, underbody shields, spoilers, etc. A third contributor is the increasing number of "what if" exploratory studies performed early in the design process when the design is relatively fluid. Licensing costs for commercial CFD solutions can become a significant constraint as the number of simulations expands. A number of alternative products (e.g., independently developed, supported and documented forks of the popular open-source OpenFOAM® toolbox [1]) have become available in recent years, offering a lower cost alternative to traditional commercial CFD products. This paper summarizes results from a broad and deep evaluation of the capability of iconCFD® to substitute for the more traditional commercial CFD solutions currently used to support vehicle aerodynamic development early in the program development cycle. Included in this study were detailed B-car, sedan, SUV and truck shapes as well as multiple variants of each shape. The study investigated both static and moving ground boundary conditions as well as alternative turbulence models. Trends of the predicted aerodynamic drag coefficients (C_d) are compared against experimental data. Both transient and steady state simulation ranking accuracy of total vehicle C_d were found to be equivalent to that historically observed with more traditional commercial solver results. A consistent upward bias in absolute C_d values was observed in the transient results.

Introduction

Aerodynamic loading on vehicles has a significant influence on fuel economy. Wind tunnel testing and computational fluid dynamics simulations are widely used to evaluate the aerodynamic forces exerted on a vehicle. There are two metrics by which the accuracy of CFD solvers have traditionally been evaluated. The first metric is visualization—the ability to accurately predict and visualize surface pressures, surface flow lines and flow field structures for potential insights into C_d reduction actions prior to test. CFD is now a widely accepted tool for this type of pretest analysis. The second metric is the absolute accuracy of the predicted aerodynamic coefficients. Numerous validation studies have been performed by both academia and automotive OEMs over the last two decades for the purpose of determining if the predictive accuracy of CFD could consistently and reliably replicate experimental results. Accuracy levels have significantly improved over the years as a function of increasing model definition, mesh resolution, etc., however, absolute replication of experimental force measurements remains somewhat challenging. It should be noted that repeatability of wind tunnel measurements between different facilities can also be an issue. In particular, test section replication, small tire modifications, etc. can have a significant effect on the measured forces.

Today's aerodynamicist continues to depend on CFD to visualize flow field data for insight into potential C_d reduction actions. As experimental aerodynamicists acknowledge that results can often be tunnel dependent and CFD proponents acknowledge that certain phenomena are extremely challenging to simulate, a third metric, ranking accuracy, has become increasingly important. Today's aerodynamicists depend on CFD to correctly rank aerodynamic coefficients across both multiple vehicle shapes and configuration variations within a given shape.

Numerically driven designed experiments and optimization studies are driving the number of CFD simulations performed to increase at a rapid rate. As High Performance Computing (HPC) resources continue to expand, the main constraint on increasing CFD simulations becomes the cost and availability of commercial CFD licenses. These cost and licensing constraints are driving an ever-increasing interest in open source CFD solvers. SAE Technical Paper 2011-01-0163 [2] was a limited investigation into the capability of open source CFD. That study reported that open source steady state simulations based on the Reynolds Averaged Navier–Stokes (RANS) approach did a good job at predicting C_d while transient simulations (detached eddy simulation; DES) were required for more accurate lift predictions. This paper expands on that material as it examines the viability of open source CFD as an alternative to today's commercial CFD solvers. The evaluation metrics used in the study were C_d ranking accuracy and flow visualization. Two questions were investigated. First, can an open source, finite volume, transient CFD code provide the same level of ranking accuracy as more traditional commercial CFD solvers? In other words, can open source transient analyses correctly rank not only different vehicle shapes but also variations in the configuration of each shape? Second, is the ranking accuracy of steady state analyses adequate enough to provide design direction early in the vehicle development process? The relative correctness of the flow structures predicted by the steady state analyses is evaluated by comparison against those from the transient analyses. The steady state simulations employed the k–ω SST turbulence model, and the transient simulations employed the Spalart–Allmaras detached eddy simulation model (SA-DES). Both turbulence models are commonly recommended for flows with large rotation, separation and reattachment. A total of 54 vehicle variants (including B-cars, sedans, SUVs and trucks) were evaluated in this study. Results from simulations were compared against results from wind tunnel experiments. Static ground wind tunnel testing was performed at the Ford Motor Company Dearborn Test Facility. Moving ground wind tunnel testing was performed at the Windshear facility in North Carolina. Images of the performance vehicle in the test section of both facilities are shown in Figure 1.



Windshear Test Facility	Dearborn Test Facility

Figure 1. Wind tunnel test facilities.

The structure of the paper is as follows. The Methods section of this paper discusses numerical methods, geometry modeling, boundary condition setup and the governing equations. Ranking accuracy and flow visualization for the total data set (as well as specific subsets of the data) are presented in the Results section of this paper. Observations and potential next steps are discussed in the Conclusion/Summary section of this paper.

Methods

There have been a growing number of validation studies published on open source CFD in recent years. Most have been limited in scope to a small number of either vehicle shapes or variants of a single shape. This paper reports the results of a study conducted across a wide range of vehicle shapes, configuration variants and boundary conditions. All CFD analyses were performed using a single common modeling and simulation best practice. A high level schematic of the process is shown in Figure 2.

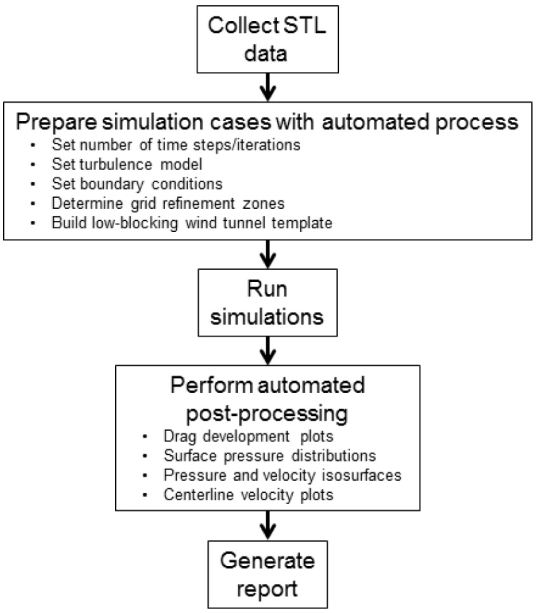


Figure 2. Schematic of the process involved in each simulation.

Numerical Method

Governing Equations

RANS Method

In the current study, the three-dimensional incompressible Reynolds Averaged Navier-Stokes (RANS) equations were used for simulating turbulent flow over different vehicles. The continuity and momentum equations used are as follows:

$$\frac{\partial \rho}{\partial t} + \frac{\partial}{\partial x_i}(\rho u_i) = 0, \tag{1}$$

$$\frac{\partial}{\partial t}(\rho u_i) + \frac{\partial}{\partial x_j}(\rho u_i u_j) = -\frac{\partial p}{\partial x_i} + \frac{\partial}{\partial x_j}\left[\mu\left(\frac{\partial u_i}{\partial x_j} + \frac{\partial u_j}{\partial x_i} - \frac{2}{3}\delta_{ij}\frac{\partial u_l}{\partial x_l}\right)\right] + \frac{\partial}{\partial x_j}\left(-\rho\overline{u_i' u_j'}\right). \tag{2}$$

In these equations u_i, p, ρ and μ represent the velocity, pressure, density and kinematic viscosity, respectively, and the overbar represents a time-averaged quantity. In RANS in order to calculate the shear stresses, the Boussinesq hypothesis (which relates the stresses to the mean velocity gradients) is used, i.e.,

$$-\rho\overline{u_i'u_j'} = \mu_t\left(\frac{\partial u_i}{\partial x_j}+\frac{\partial u_j}{\partial x_i}\right)-\frac{2}{3}\left(\rho k+\mu_t\frac{\partial u_k}{\partial x_k}\right)\delta_{ij} \quad (3)$$

where μ_t is the turbulent viscosity, k is the turbulent kinetic energy and ϵ is the dissipation rate. Among the RANS turbulence models available, the Spalart-Allmaras, k–ϵ and k–ω use the Boussinesq hypothesis. These approaches are employed when low computational cost is required.

For the RANS portion of this study, Menter's k–ω SST model was used [3]. The k–ω SST model is designed in a way to activate the standard k–ω model in the inner region of the boundary layer and the standard k–ϵ model in the outer region. It also uses a modified turbulent viscosity equation to take into consideration the transport effects of the shear stresses. In this model the turbulent viscosity is calculated from

$$\mu_t = \left(\frac{\rho k}{\omega}\right).\left(\frac{1}{\max\left[\frac{1}{\alpha^{**}},\frac{SF_2}{a_1\omega}\right]}\right) \quad (4)$$

where F2 is a blending function, s is the strain-rate magnitude, α_1 =0.31 and α* is given by

$$\alpha^* = \alpha_\infty^*\left(\frac{\alpha_0^*+\frac{Re_t}{R_k}}{1+\frac{Re_t}{R_k}}\right) \quad (5)$$

where

$\alpha_0^* = 0.024$, $R_k = 6.0$, $Re_t = \left(\frac{\rho k}{\mu\omega}\right)$, $\alpha^* = \alpha_\infty^* = 1$ in high-Re flows and ω is the turbulence specific dissipation rate. These features make the k–ω SST model more robust and accurate for flows with adverse pressure gradients and separation and reattachment comparing to the standard case.

Second-order spatially accurate schemes were used to discretize the governing RANS equations within the framework of the finite volume method (FVM). The SIMPLEC algorithm is used for pressure-velocity coupling, and iconCFD's *iconSimplecFoam* version 3.0.17, based on OpenFOAM's *simpleFoam*, was used to solve the governing equations. The RANS simulations were run for about 3000 iterations each on 144 processors on high performance computing clusters, and the combined meshing and simulation time for each case was approximately 12 hours. The behavior of the drag force on the vehicles was monitored, and the solution was assumed to be finalized and converged when the drag coefficient exhibited either a repeatable behavior or showed no significant change with each successive iteration. Based on this criterion, the simulations were observed to be converged before reaching the above mentioned iteration number.

DES Method

Three-dimensional incompressible DES simulations were also carried out to solve the transient flow over different vehicles. DES is a hybrid method which combines the benefit of using RANS-based methods in the wall proximity region and LES in the rest of the domain. The popularity of this method is growing rapidly for many industrial applications due to its comfort for satisfying the mesh requirements compared to the LES method. The DES approach used in the current analyses employs a filtered approach where the sub-grid scale model used is the Spalart–Allmaras turbulence model with a higher influence near the wall and a decay far from the wall.

As with the RANS simulations, a second-order finite volume discretization was used. Second-order temporal discretization was also employed, and the PISO algorithm was used for pressure-velocity coupling. A time step of 0.0001 seconds was chosen for the transient cases, and simulations were conducted on 144 and 240 cores on the HPC system. Transient simulations were run for 1.5 seconds of simulated time (which corresponded to 3-5 days of wall clock time), and statistical averages were computed over the last 1.0 seconds of simulated time.

Determination of the ranking accuracy of the predicted aerodynamic drag coefficient was the primary focus of the study. Flow field visualization comparisons were conducted in order to confirm the correctness of the solution and inspect for possible offsetting errors.

Geometry Modeling and Boundary Conditions

An example of one geometry modelled in the current study is presented in Figure 3. The size of the domain is kept constant in all cases and only the vehicle is changed. To minimize the influence of the inlet, outlet, sides and top boundaries on the pressure and velocity fields, the computational domain is considered to be 60 m in length, 50 m in width and 30 m in height. Based on this dimensions, the maximum blockage ratio for all vehicles analyzed is between 1.5% to 2.5%, which is smaller than the 3% maximum suggested by Franke et al. [4]. Note that a constant numerical setup was applied to all cases.

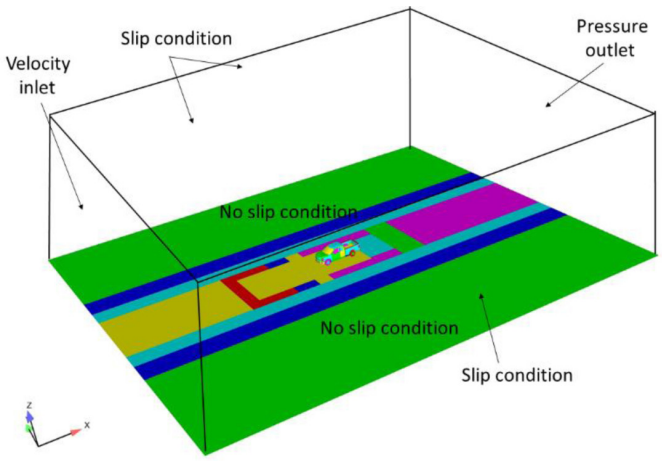


Figure 3. Computational domain and boundary conditions.

For consistency, a single user independent meshing strategy was applied to all vehicle models. iconCFD's hexahedral dominant unstructured mesh generator *iconHexMesh*, derived from OpenFOAM's *snappyHexMesh*, was used for creating the hybrid mesh inside the domain. There are different approaches in CFD for

accounting the wall effect. In the current study, the wall function approach, which uses the law of the wall, was used for modeling the flow in the wall region. This approach was used for both k–ω SST and DES methods. In order to use a wall function, a grid spacing with $30 < y^+ < 300$ is required. Here, $y^+ = u_\tau y/\nu$ is a non-dimensional wall distance, where $u_\tau = (\tau_w/\rho)^{0.5}$ is the friction velocity, y is the wall normal distance, ν is the kinematic viscosity, ρ is the density and τ_w is the wall shear stress.

In order to capture the influence of the high velocity gradients in the wall regions, a finer mesh is used for regions close to the walls (ground surface and vehicle parts); while for the rest of the domain, a coarser mesh is used. Cells adjacent to most parts of the vehicle were refined 9 times, with cells next to finer-detailed parts such as tires and grilles being refined 10 times. Near all vehicle parts a boundary layer mesh with 6 high aspect ratio layers was generated with an expansion ratio of approximately 1.3, such that the first cell center was located in the log law region of the boundary layer, consistent with the high Reynolds number wall function strategy. Additional refinement regions were added to capture the vehicle wake, an example of which is shown in Figure 4. On average, the vehicle models were simulated with about 15 million surface mesh elements, and the entire computational domain contained approximately 100 million volume mesh elements.

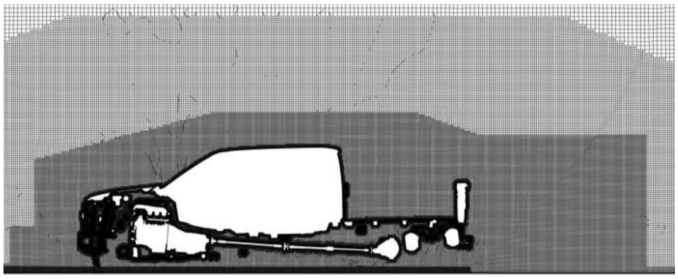


Figure 4. Constructed mesh around a model.

The boundary conditions considered include a constant velocity of 80 mph at the inlet with a turbulence intensity of 0.5%, which matches the wind tunnel condition. A symmetry boundary condition is applied to both the top and side walls. The ground surface is split two sections, one with slip condition and the other with the no-slip condition. In order to consider the boundary layer growth in the upstream of the domain, a distance of 9.6m in the upstream ahead of the vehicle is set to have no-slip condition. For the rest of the ground surface, a slip condition is used. A pressure outlet condition that lets the flow to exit to the atmosphere is applied at the outlet. For static ground cases, static boundary conditions were used on the floor and the tires. For other cases, in order to correctly consider the car movement, moving ground and rotating tire boundary conditions were used. The numerical wind tunnel was tuned to generate measured empty tunnel boundary layer growth for static conditions in order to best replicate wind tunnel measurements.

Table 1. Summary of validation models.

Model #	Test condition	Steady State (RANS)	Transient (DES)
		Turbulence model	
		k–ω SST	SA
1	DrivAer-fastback-smooth floor	√	√
2	DrivAer -notchback-smooth floor	√	√
3	DrivAer -fastback-detailed floor	√	√
4	DrivAer -notchback-detailed floor	√	√
5	DrivAer-wagonback-smooth floor	√	√
6	DrivAer-wagonback-detailed floor	√	√
7	Sedan 1-closed grille-static ground	√	√
8	Sedan 1-closed grille-moving ground	√	√
9	Sedan 1-closed AGS-static ground	√	√
10	Sedan 1-closed AGS-moving ground	√	√
11	Sedan 1-open AGS-static ground	√	√
12	Sedan 1-open AGS-moving ground	√	√
13	Sedan 1-closed AGS-no shield-static ground	√	√
14	Sedan 1-closed AGS-no shield-moving ground	√	√
15	Sedan 2-closed grille-static ground	√	√
16	Sedan 2-closed grille-moving ground	√	√
17	Sedan 2-closed AGS-static ground	√	√
18	Sedan 2-closed AGS-moving ground	√	√
19	Sedan 2-open AGS-static ground	√	√
20	Sedan 2-open AGS-moving ground	√	√
21	Sedan 3-closed AGS-mirrors off-static ground	√	√
22	Sedan 3-closed AGS-center suspension shield removed-static ground	√	√
23	Sedan 3-closed AGS-baseline-static ground	√	√
24	Sedan 3-closed AGS-engine extension shield removed-static ground	√	√
25	Sedan 3-closed AGS-rocker shields removed-static ground	√	√
26	Sedan 3-closed AGS-engine shield removed-static ground	√	√
27	Sedan 3-closed AGS-belly pan and tire spoiler removed-static ground	√	√
28	Performance vehicle-closed grille-moving ground	√	√
29	Performance vehicle-closed AGS-static ground	√	√
30	Performance vehicle-closed AGS-moving ground	√	√
31	Performance vehicle-open AGS-static ground	√	√
32	SUV-closed grille-static ground	√	√
33	SUV-closed AGS-static ground	√	√
34	SUV-closed AGS-moving ground	√	√
35	SUV-open AGS-static ground	√	√
36	SUV-open AGS-moving ground	√	√
37	B-car-mirrors off-static ground	√	√
38	B-car-baseline-static ground	√	√
39	B-car-speedlip off-static ground	√	√
40	B-car SUV-mirrors off -static ground	√	√
41	B-car SUV-baseline-static ground	√	√
42	B-car SUV-speedlip off-static ground	√	√
43	Truck 1-chin spoiler-static ground	√	√
44	Truck 1-airdam-static ground	√	√
45	Truck 1-baseline-static ground	√	√
46	Truck 2-closed grille-static ground	√	√
47	Truck 2-closed AGS-static ground	√	√
48	Truck 2-closed AGS-moving ground	√	√
49	Truck 2-open AGS-static ground	√	√
50	Truck 2-open AGS-moving ground	√	√
51	Truck 2-closed AGS-tailgate down-static ground	√	√
52	Truck 2-closed AGS-tailgate down-moving ground	√	√
53	Truck 2-closed AGS-tailgate off-static ground	√	√
54	Truck 2-closed AGS-tailgate off-moving ground	√	√

Validation Models

The objective of this study was to determine the capability of an open-source CFD solver to support aerodynamic development across all vehicle programs. It was therefore necessary to evaluate the solver across a wide range of vehicle shapes and variants. Detailed B-car, sedan, SUV and truck shapes, as well as multiple variants of each shape, are included in this study. A select set of simplified models (DrivAer notchback, fastback and wagonback) are also included [5]. A summary of all cases simulated and their setup information is provided in Table 1.

Model Geometry

Model geometry for each of the base models are presented in Figure 5. The details of each model variant are presented in Figure 5 to Figure 15.

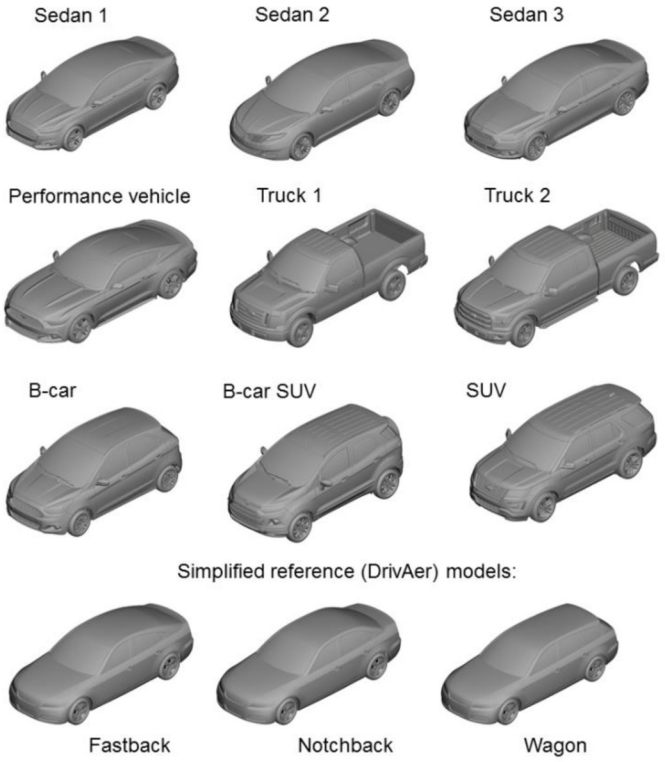


Figure 5. Validation set of base models.

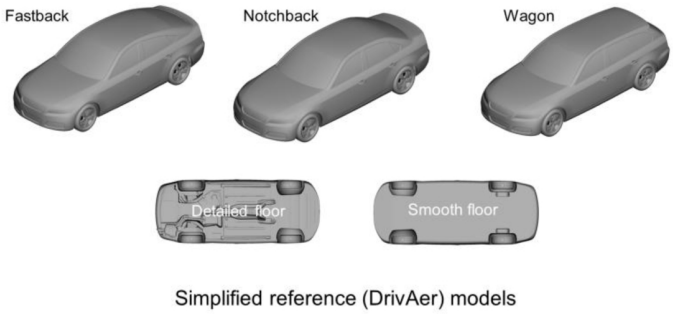


Figure 6. DrivAer models with configuration variants.

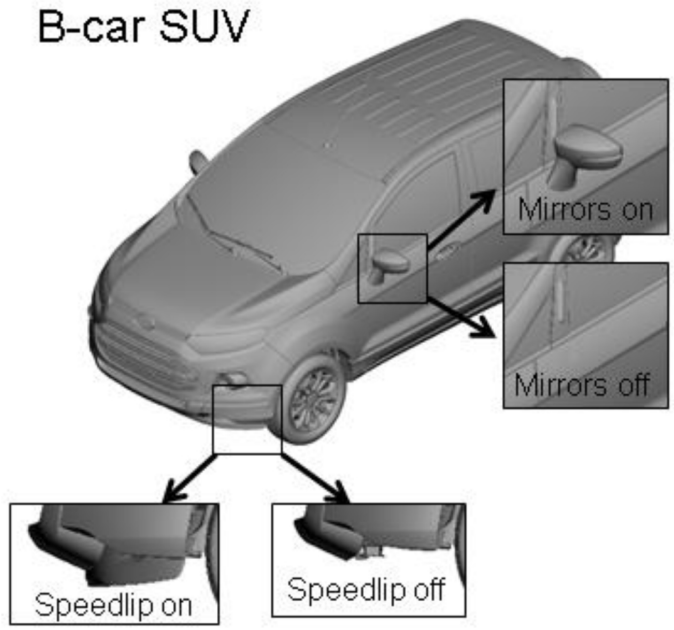


Figure 7. B-car SUV base model and configuration variants.

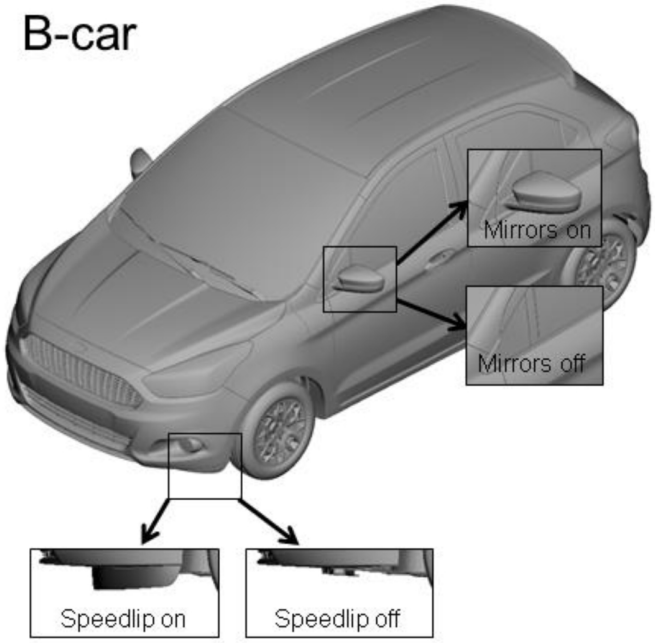


Figure 8. B-car base model and configuration variants.

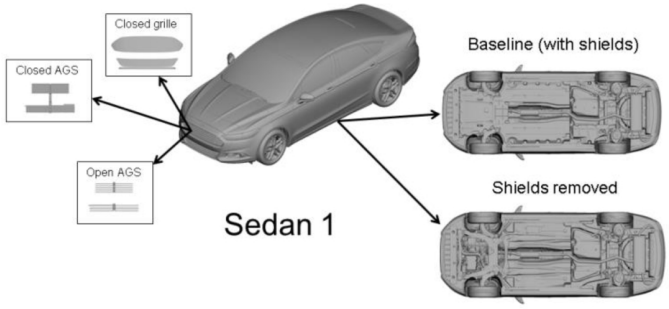


Figure 9. Sedan 1 base model and configuration variants.

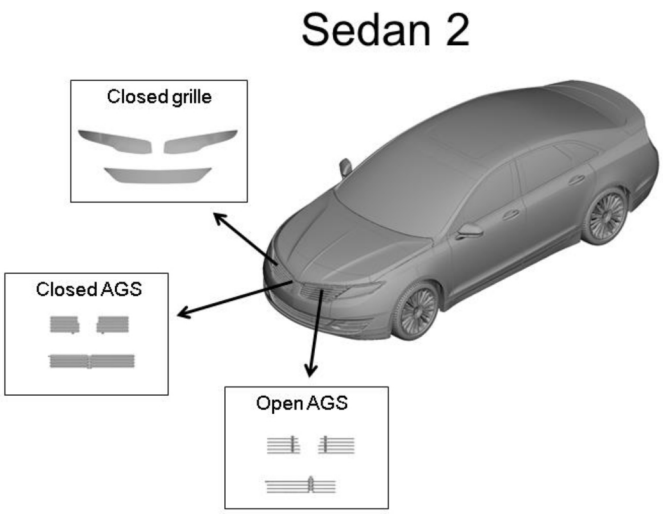


Figure 10. Sedan 2 base model and configuration variants.

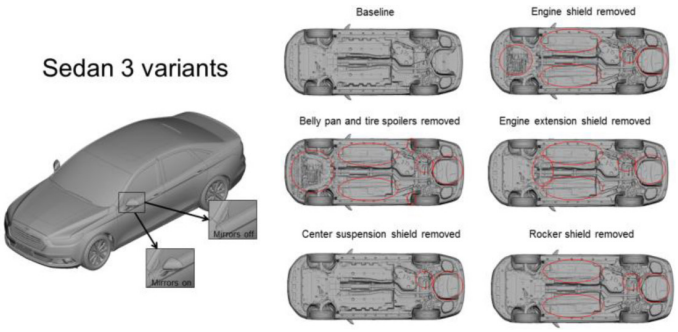


Figure 11. Sedan 3 base model and configuration variants.

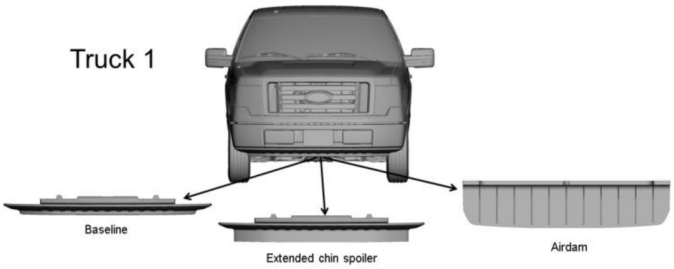


Figure 12. Truck 1 base model and configuration variants.

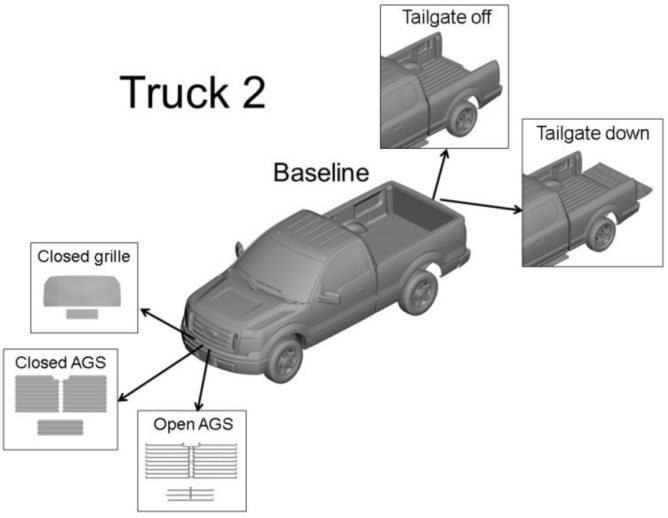


Figure 13. Truck 2 base model and configuration variants.

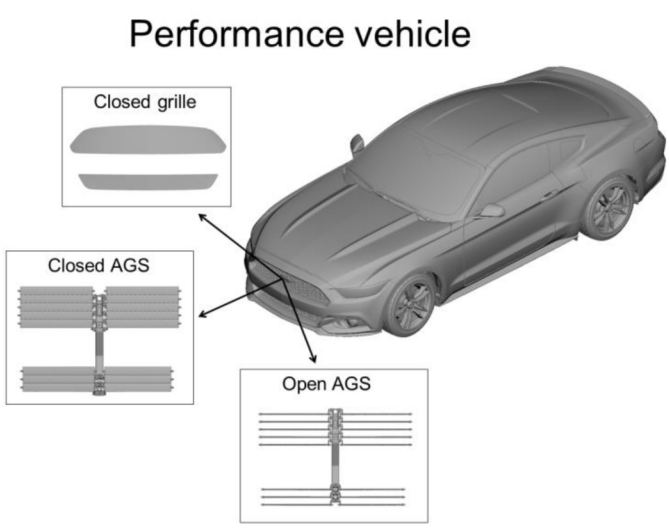


Figure 14. Performance vehicle base model and configuration variants.

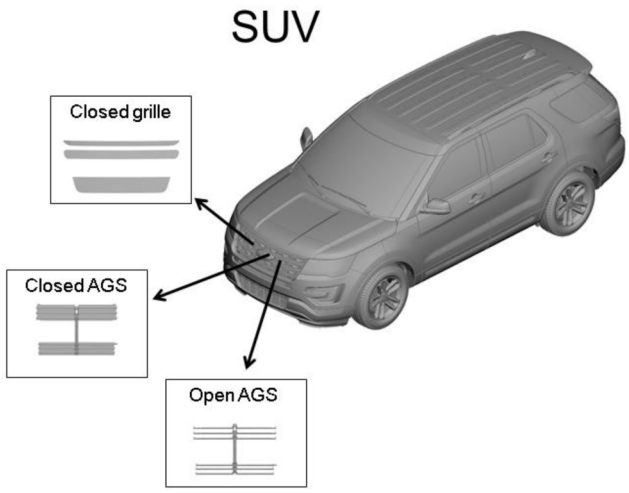


Figure 15. SUV base model and configuration variants.

Metrics

C_d ranking accuracy is the primary metric for comparing simulated and measured results. It provides a measure of the capability of the simulation tool to correctly predict the C_d trends across the vehicle sample set used in this study. C_d development plots and flow visualization were used to identify any significant differences between the steady state and transient simulation results.

C_d Ranking Accuracy

In this paper ranking accuracy is defined as the number of correctly predicted positional rankings divided by the total number of positional rankings. A visual example is presented in Figure 16. The blue bars show five sample measurements of increasing value. The red line shows the predicted values for each sample measurement. Each measurement has a rank order position relative to the other four samples, leading to a total of 20 positional rankings for this data set. The rank order of samples 1, 2 and 3 were correctly predicted four times. The rank order of samples 4 and 5 were correctly predicted three times. The net result is a total of 18 correctly predicted sample rank orders and a ranking accuracy of 90%.

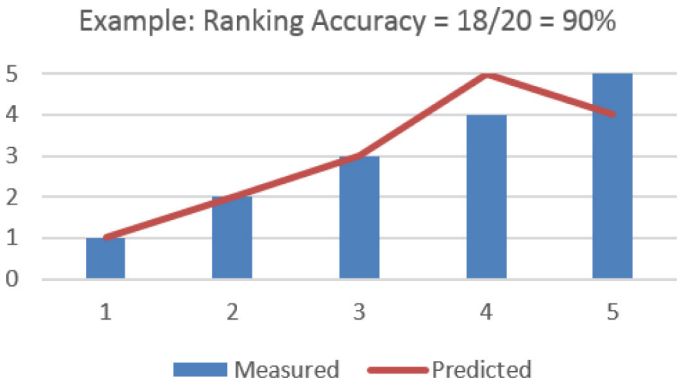


Figure 16. Ranking accuracy example.

Two metrics are used in this paper to compare the results of the steady state and transient simulations.

C_d Development Plots

The first comparison metric is the C_d development plot, an example of which is given in Figure 17. This plot is essentially a visual representation of drag accumulation moving from the front to the rear of the vehicle. This plot is used to assist in identifying locations on the vehicle with notable differences between steady state and transient local drag force predictions.

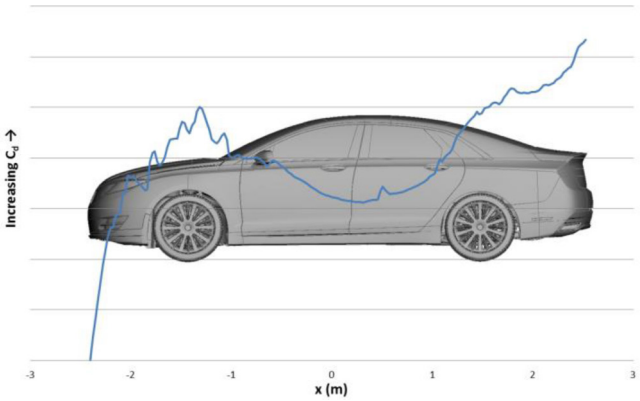


Figure 17. C_d development plot example.

Flow Visualization

The second comparison metric used in identifying significant differences between steady state and transient simulation results is flow visualization. A combination of velocity distributions and isosurfaces of wake structure were used in this study.

Results

A total of 54 unique vehicle and vehicle variants were evaluated. C_d trends versus experimental measurements are plotted in Figure 18. A positive bias in the absolute C_d values was observed in both the transient and steady state simulation results. The values in the plot have been adjusted by subtracting the average bias from the drag values. The simulation results reveal a high level of correlation to the experimental trends for both the transient and steady state results.

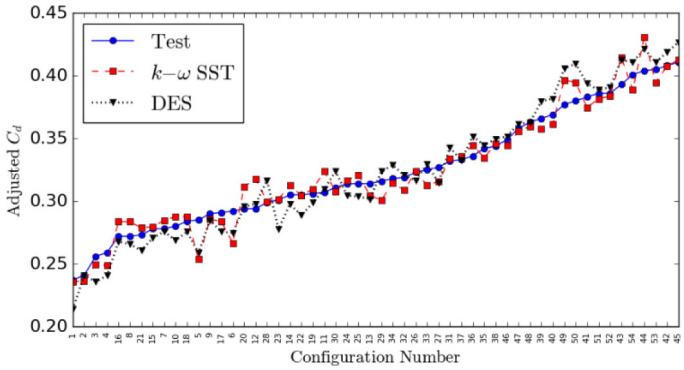


Figure 18. Normalized C_d trend predictions versus experimental measurements.

Cd Ranking Accuracy - All Cases

The correlation presented in Figure 18 is further supported by the ranking accuracy bar graph shown in Figure 19. The steady state and transient ranking accuracy results from the entire data set were very good and generally equivalent to similar studies performed on commercial CFD solver applications.

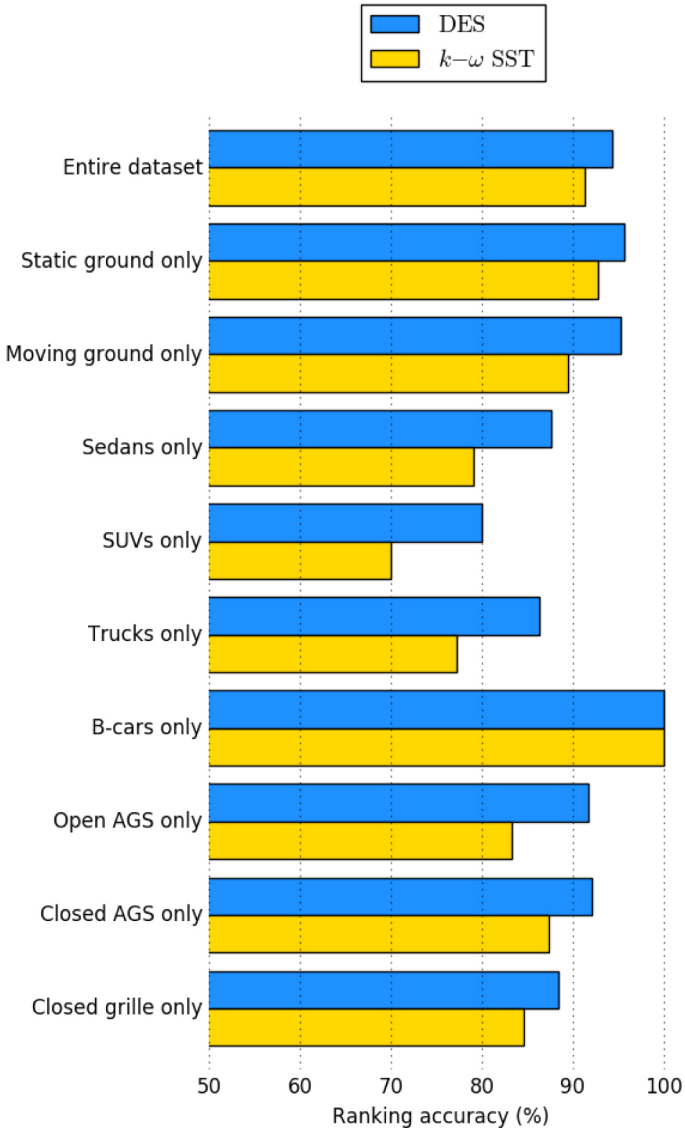


Figure 19. Steady state and transient C_d ranking accuracy for all data sets.

As Figure 19 shows, the ranking accuracy for the transient results was 94.3%, while the ranking accuracy for the steady state results was 91.3%. The ranking accuracies of both methods were approximately equivalent overall, and were in alignment by expectations based on previous results from more traditionally utilized commercial solvers. The broad range of shapes and boundary conditions within the data set, however, creates the potential for making lower accuracy results within subsets of the data. To that extent, the data was divided into different specific groupings as following and the ranking accuracies recalculated for each case:

1. Static Ground
2. Moving Ground
3. Sedans
4. SUVs
5. Trucks
6. Open AGS
7. Closed AGS
8. Closed Grille
9. B-cars

A total of 39 samples were included for the static ground cases, 15 for the moving ground cases, 21 for sedans, 5 for SUVs, 12 for trucks, 6 for B-cars, 9 for open AGS, 23 for closed AGS and 13 for closed grille cases. The following observations were made:

- Ranking accuracy for the static ground cases was equal or slightly higher than the ranking accuracy calculated for the entire data set. DES results were 1.4% greater. Results from the k–ω SST model simulations were 1.4% greater.
- For the moving ground cases, the ranking accuracy was approximately equal to the number calculated for the entire data set. DES results were 0.9% greater. k–ω SST results were 1.8% less.
- For sedan cases the ranking accuracy number was lower than the one calculated for the entire data set. DES results were 6.7% lower. k–ω SST results were 12.3% lower.
- Ranking accuracy for the SUV subset of cases was lower than the ranking accuracy calculated for the entire data set. DES results were 14.3% lower. k–ω SST results were 21.3% lower.
- DES ranking accuracy for the truck subset of cases, at 86.4%, was 7.9% lower than the ranking accuracy of the entire data set. k–ω SST ranking accuracy, at 77.3%, was 14.0% lower.
- For the open AGS cases the ranking accuracy was slightly lower than the ranking accuracy calculated for the entire data set. DES results were 2.6% lower. k–ω SST results were 8% lower.
- Ranking accuracy for the closed AGS subset of cases was slightly lower than the ranking accuracy calculated for the entire data set. DES results were 2.2% lower. k–ω SST results were 3.9% lower.
- Ranking accuracy for the closed grille subset of cases was slightly lower than the ranking accuracy calculated for the entire data set. DES results were 5.8% lower. k–ω SST results were 6.7% lower.
- Ranking accuracy for the B-car subset of cases was higher than the ranking accuracy calculated for the entire data set. DES results were 5.7% higher. k–ω SST results were 8.7% higher. The 100% ranking accuracies are most likely an anomaly attributable to the small size of the subset and to the types of variants included in the subset.

C_d Development Plots - Static Ground Cases

C_d development plots for the 12 base models simulated with static ground conditions (with both the k–ω SST and DES turbulence models) are presented in Figure 20 to Figure 31. The experimentally measured total vehicle C_d is included for reference in each plot.

Key observations:

1. Both DES and k–ω SST closed front end simulations generated similar results (Figure 20 to Figure 22) from the front bumper to the midpoint of the wheelbase ($x = 0$).
2. Both DES and k–ω SST open front end simulations (Figure 23 to Figure 31) generated similar results from the front bumper to the heat exchangers.
3. Both turbulence models capture the same overall C_d development pattern in the under hood region, although some differences are seen in absolute C_d values predicted in that region.
4. C_d development patterns were similar for most vehicles from the rear of the engine compartment to the B-pillar with the exception of the performance vehicle (Figure 29). Further investigation is required to understand the mechanisms behind these differences.
5. C_d development with the DES model increased at a slightly greater rate than the k–ω SST model between the B-pillar and the rear corners of the models. Initial review of the flow fields indicate that this may be the result of differences in underbody flow rates.
6. No consistent pattern in the C_d development differences between DES and k–ω SST simulations was observed in the data at the base of the models. This result is not totally unanticipated given the complexity of the flow field in that region.
7. A positive bias in the DES predicted total vehicle C_d is observed in the data.

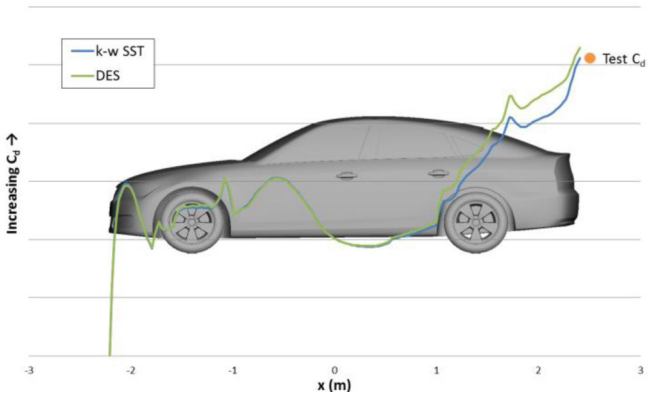


Figure 20. C_d development plot for the fastback variant of the simplified reference model (detailed floor, static ground condition).

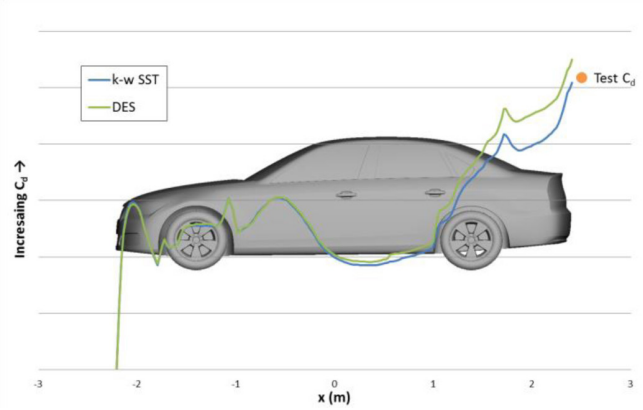


Figure 21. C_d development plot for the notchback variant of the simplified reference model (detailed floor, static ground condition).

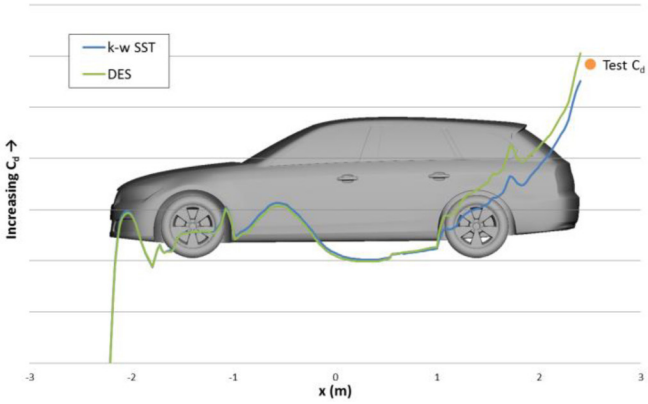


Figure 22. C_d development plot for the wagonback variant of the simplified reference model (detailed floor, static ground condition).

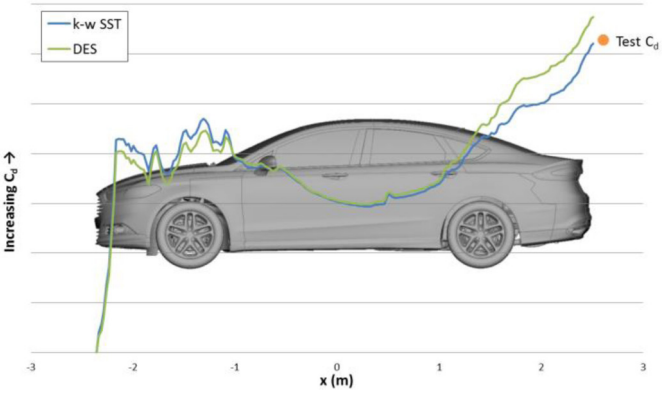


Figure 23. C_d development plot for Sedan 1 (closed AGS, shields removed, static ground condition).

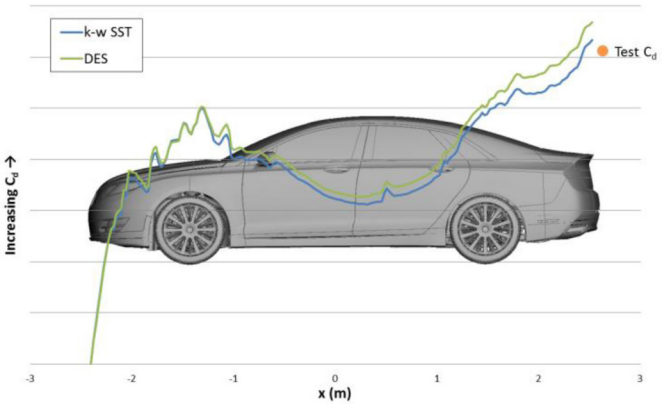


Figure 24. C_d development plot for Sedan 2 (open AGS, static ground condition).

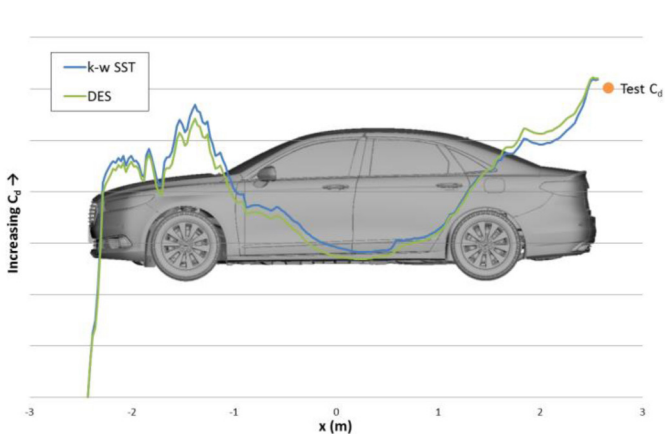


Figure 25. C_d development plot for Sedan 3 (baseline, static ground condition).

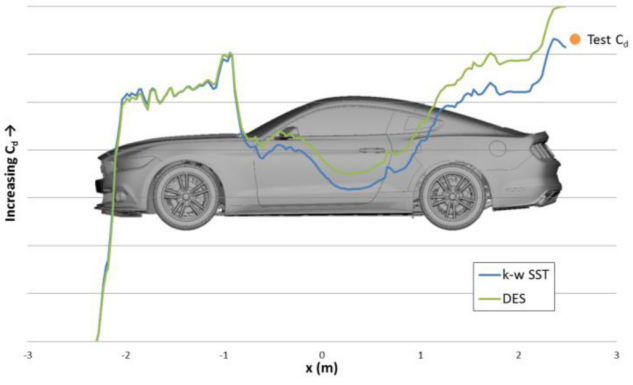


Figure 26. C_d development plot for the performance vehicle (closed AGS, static ground condition).

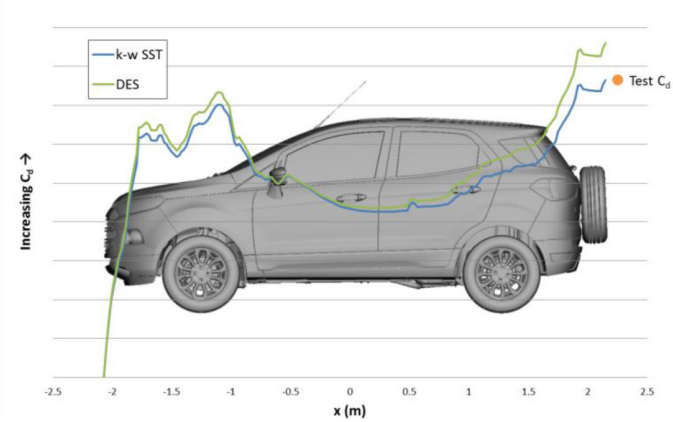


Figure 27. C_d development plot for the B-car SUV (baseline, static ground condition).

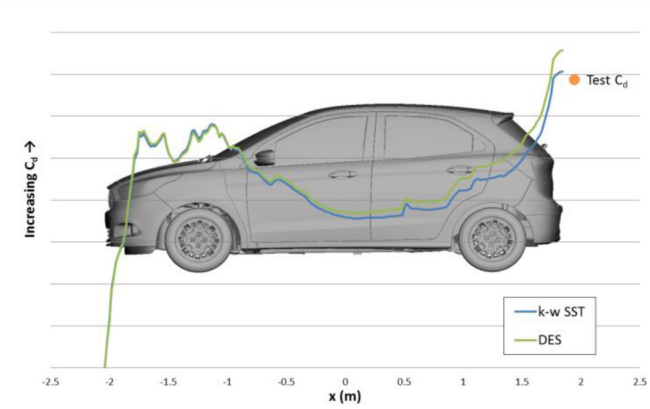


Figure 28. C_d development plot for the B-car (baseline, static ground condition).

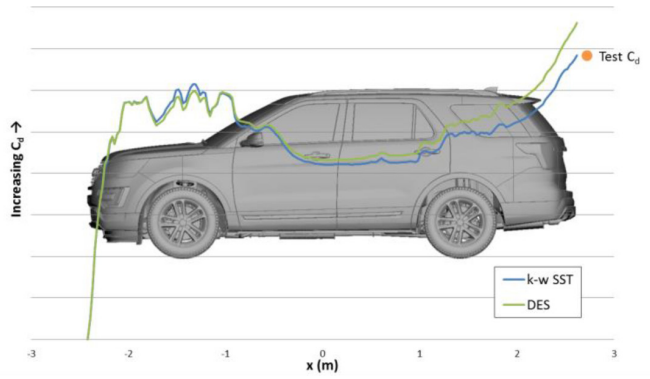


Figure 29. C_d development plot for the SUV (open AGS, static ground condition).

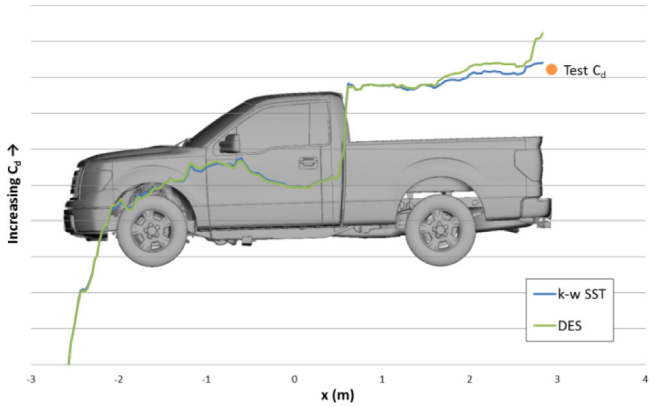


Figure 30. C_d development plot for Truck 1 (baseline, static ground condition).

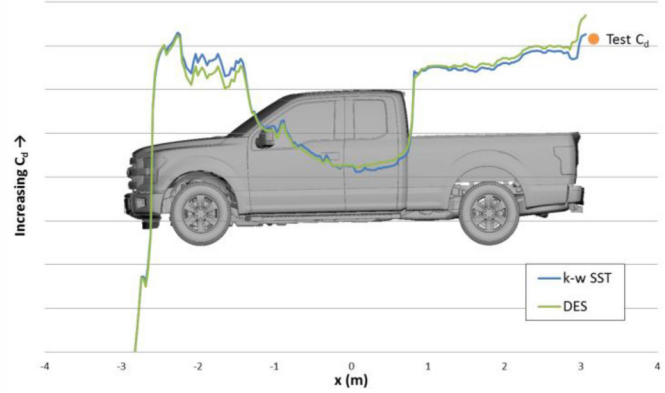


Figure 31. C_d development plot for Truck 1 (closed AGS, static ground condition).

Flow Visualization - Static Ground Cases

Isocontours of zero total pressure for the 12 base models simulated with static ground conditions (with both k–ω SST and DES turbulence models) are shown in Figure 32 and Figure 33. Centerline velocities (with the colorbar scale indicating the velocity magnitude in meters per second) for the 12 base models are displayed in Figure 34 and Figure 35. These figures are useful in highlighting the differences in the predicted flow structures around vehicles.

Key observations:

1. Based on these evaluations, the RANS-based k–ω SST creates larger separation vortices (as compared to the transient DES model) around tires. The k–ω SST model also creates wall-attached vortices in the wake region.
2. It can be realized from the figures that the RANS-based k– ω SST model creates higher underbody velocities.
3. For Sedan 1, 2 and 3, higher underbody velocities are observed (marked with arrows in Figure 34) using the k–ω SST model, as compared to the DES cases. This might be a possible reason for the larger separation vortices from the front tires observed in Figure 32. Low velocity regions can be seen over the backlight in all three Sedans (k–ω SST cases). This is consistent with the separation bubbles observed in that region.
4. The velocity contours for the SUV obtained from two models are similar, except for the mid-underbody (marked with arrows in Figure 34), where k–ω SST predicts much lower velocity.
5. For Truck 1 and 2, higher underbody velocities can be observed using k–ω SST model (marked with arrows in Figure 34). Similar to the phenomenon observed for SUV vehicles, low velocities can be seen in the mid-underbody region (marked with arrows in Figure 34) using the k–ω SST model.

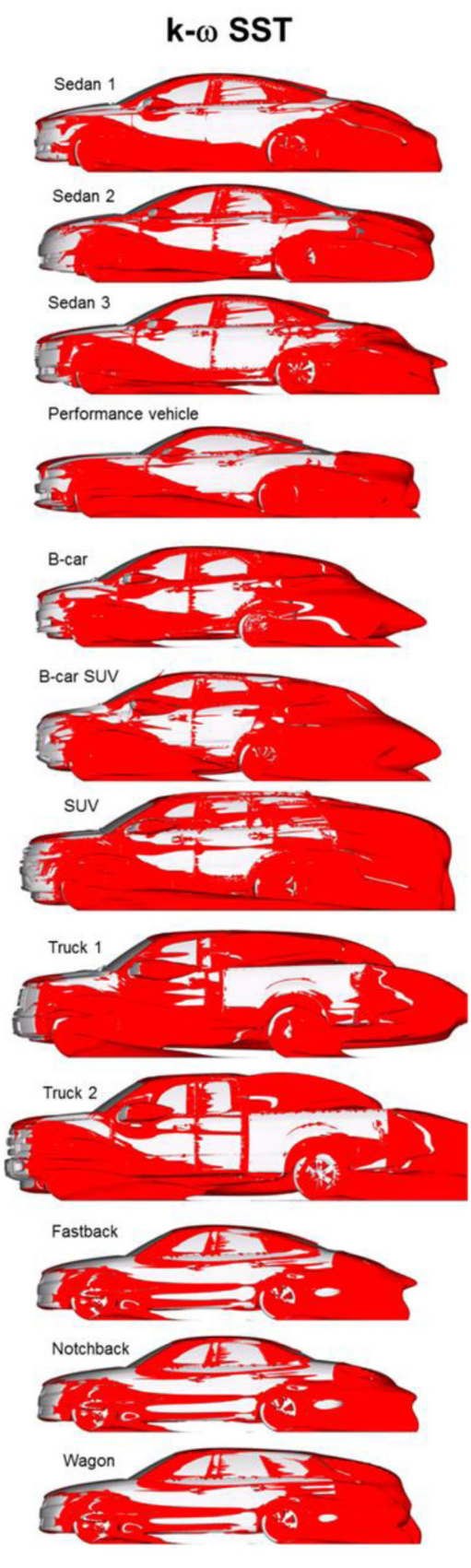


Figure 32. Isocontours of zero total pressure generated using the steady, k–ω SST turbulence model for static ground cases.

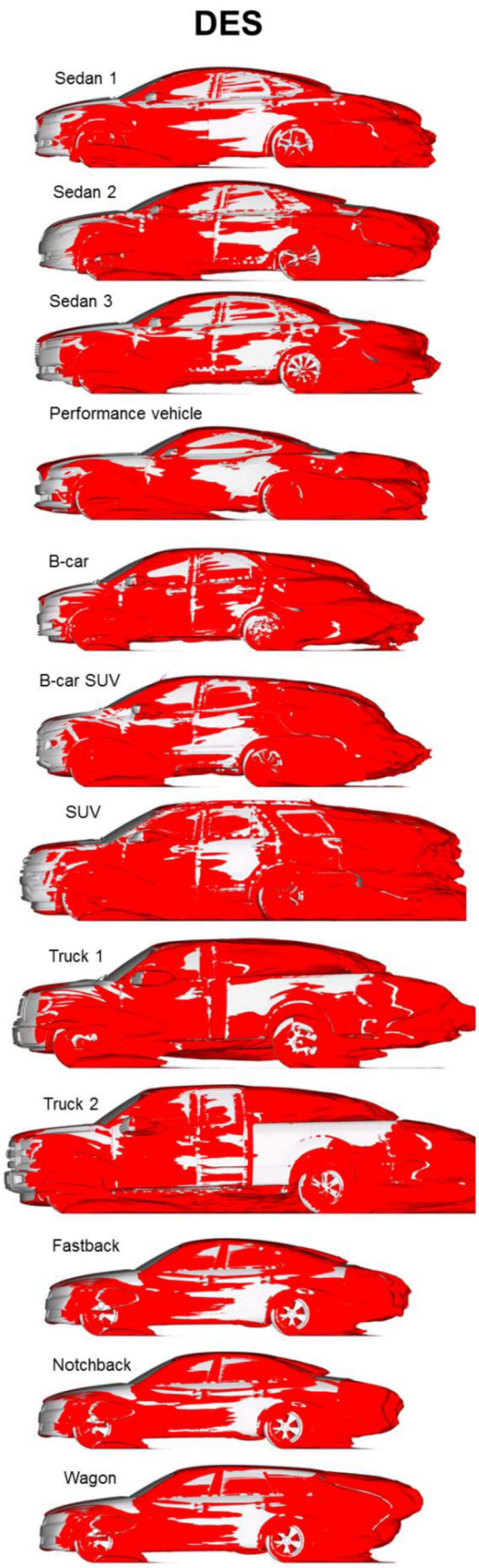


Figure 33. Isocontours of zero total pressure generated using the unsteady, DES turbulence model for static ground cases.

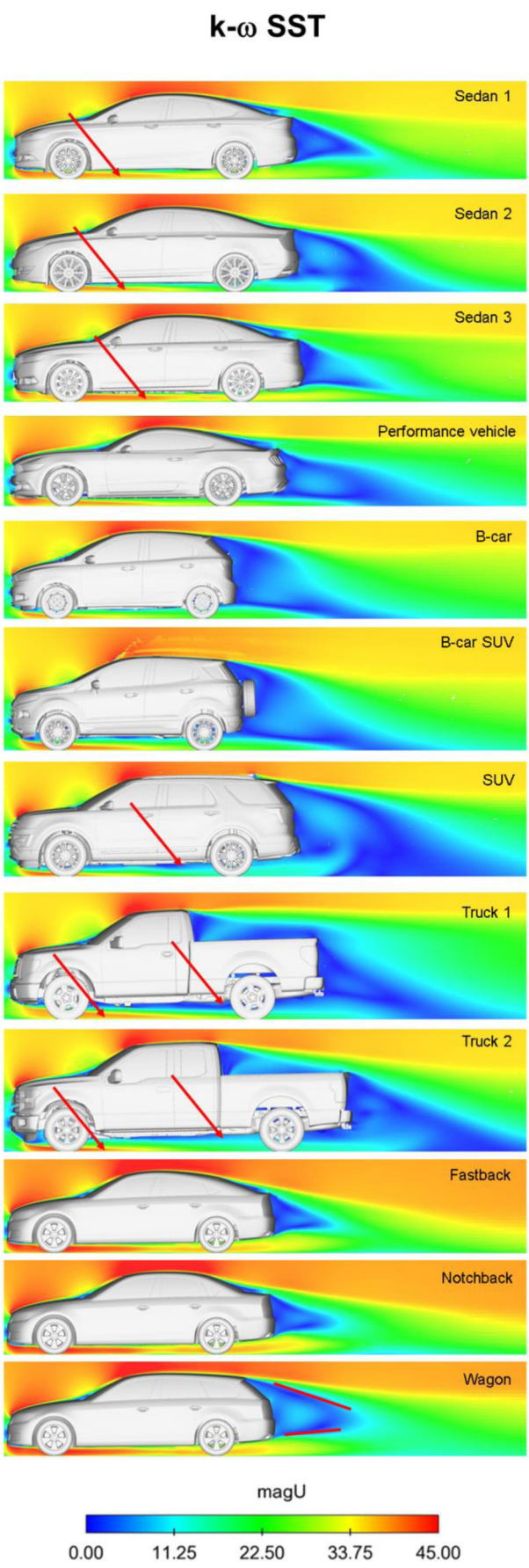


Figure 34. Contours of velocity magnitude generate using the steady, *k-ω* SST turbulence model for static ground cases.

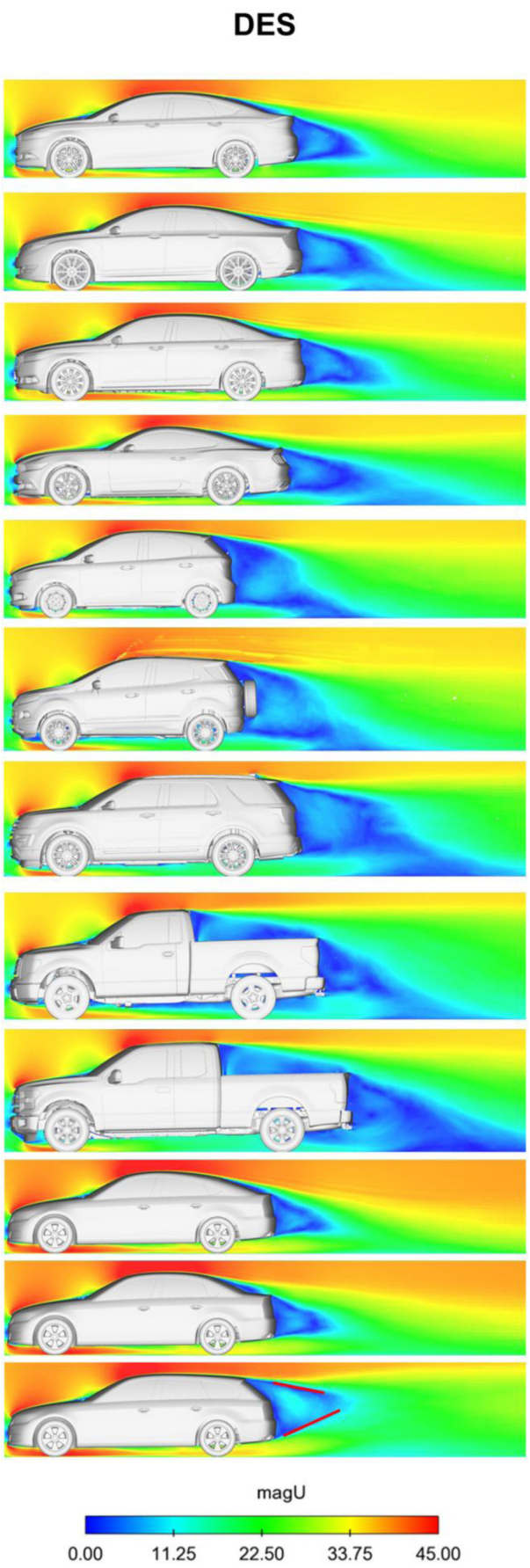


Figure 35. Contours of velocity magnitude generated using the unsteady, DES turbulence model for static ground cases.

C_d Development Plots - Moving Ground Cases

C_d development plots for the 5 base models simulated with moving ground conditions (with both k–ω SST and DES turbulence models) are presented in Figure 36 to Figure 40. The experimentally measured total vehicle C_d is included for reference in each plot.

Key observations:

1. Both DES and k–ω SST open front end simulations generated similar results from the front bumper to the heat exchangers (Figure 36 to Figure 40).
2. Both turbulence models capture the same overall C_d development pattern in the under hood region, although some differences are seen in absolute C_d values predicted in that region (Figure 36 to Figure 40).
3. C_d development patterns were similar for most vehicles from the rear of the engine compartment to the B-pillar. DES and k–ω SST patterns for the performance vehicle (Figure 38) showed less variation than that seen under static ground conditions.
4. C_d development with the DES model increased at a slightly greater rate than the k–ω SST model beginning at the C-pillar.
5. C_d development differences between DES and k–ω SST simulations observed at the base of the models were much less than those observed under static ground conditions.
6. A positive bias in the DES predicted total vehicle C_d is observed in the data similar to that noted in the static ground simulations.

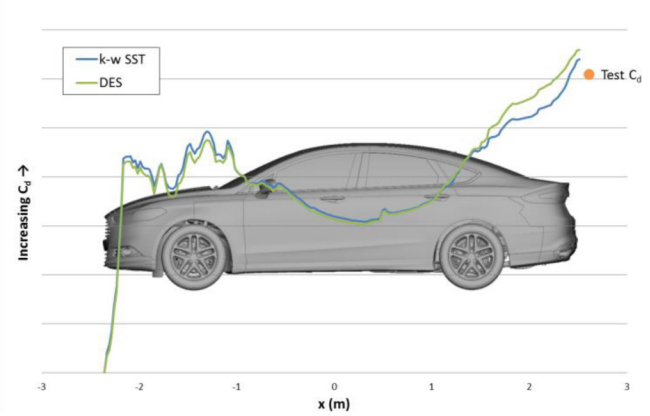


Figure 36. C_d development plots for Sedan 1 (closed AGS, shields removed, moving ground condition).

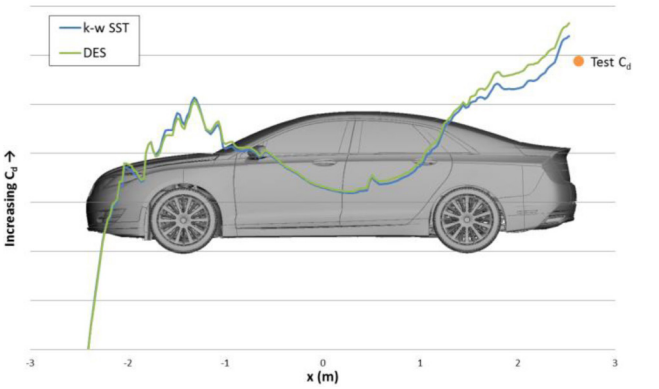


Figure 37. C_d development plots for Sedan 2 (open AGS, moving ground condition).

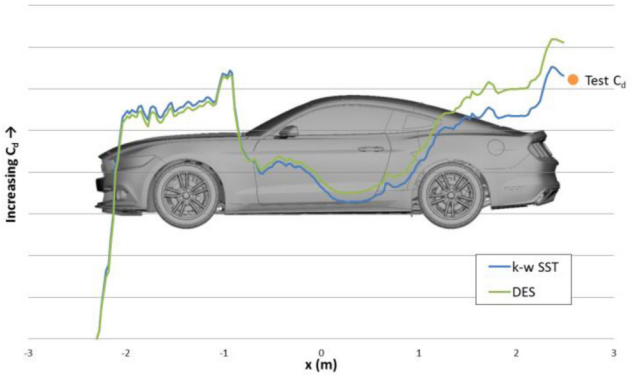


Figure 38. C_d development plots for performance vehicle (closed AGS, moving ground condition).

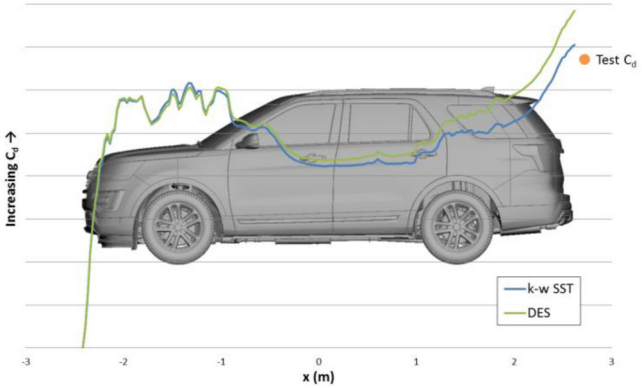


Figure 39. C_d development plots for SUV (open AGS, moving ground condition).

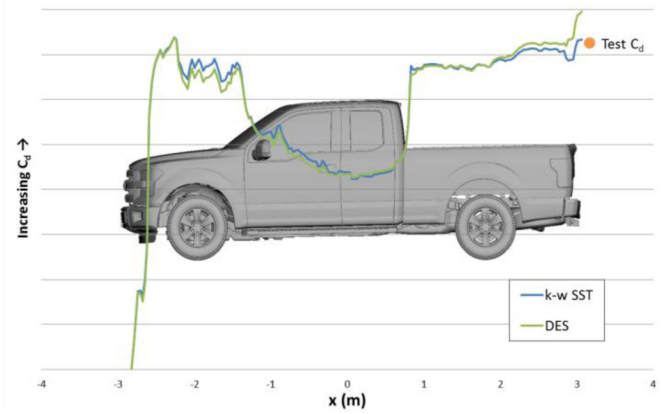


Figure 40. C_d development plots for Truck 2 (closed AGS, moving ground condition).

Flow Visualization - Moving Ground Cases

Isocontours of zero total pressure for the five selected vehicles (Sedan 1 and 2, the performance vehicle, the SUV and Truck 2) simulated with moving ground conditions (with both k–ω SST and DES models) are shown in Figure 41 and Figure 43. Figure 42 and Figure 44 show the centerline velocity magnitude contours.

The key observations from these figures were:

1. For all five vehicles, larger separation vortices from the front tires can be observed using the k–ω SST model compared to those from the DES model.
2. For all five vehicles, higher underbody velocities are observed (marked with arrows in Figure 42) using the k–ω SST model as compared to DES.
3. The k–ω SST model predicts lower velocities for regions close to the mid-underbody for the SUV and Truck 2 (marked with arrows in Figure 42).

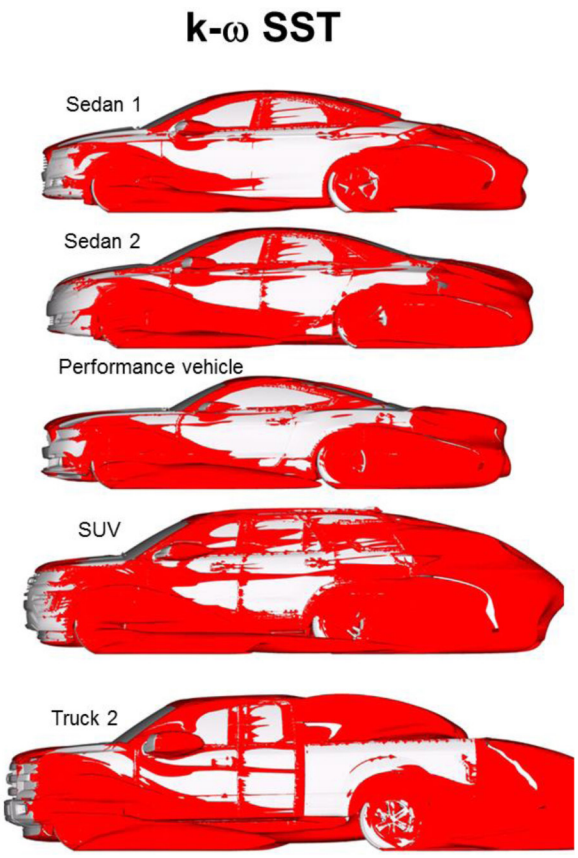


Figure 41. Isocontours of zero total pressure generated using the steady, *k–ω* SST turbulence model for moving ground cases.

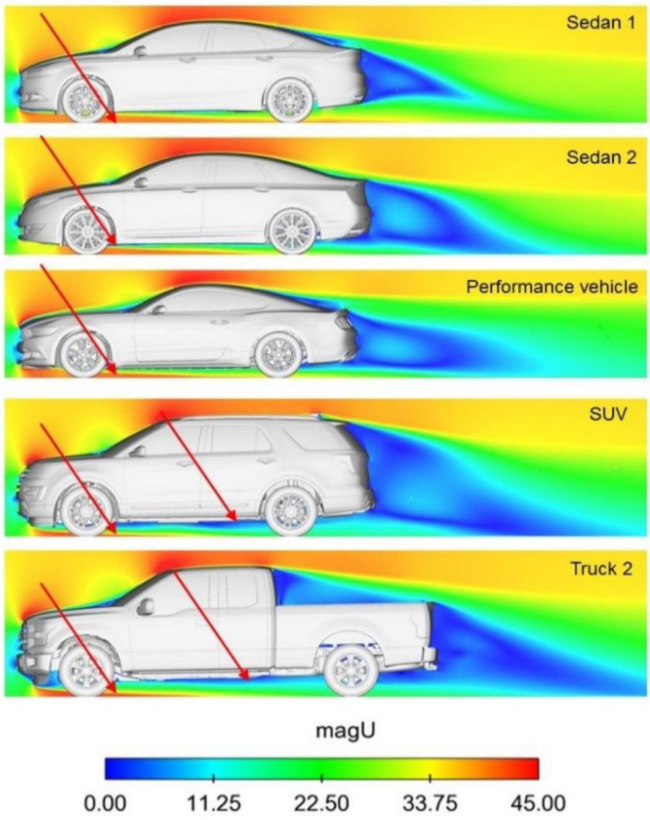


Figure 42. Contours of velocity magnitude generated using the steady, k–ω SST turbulence model for moving ground cases.

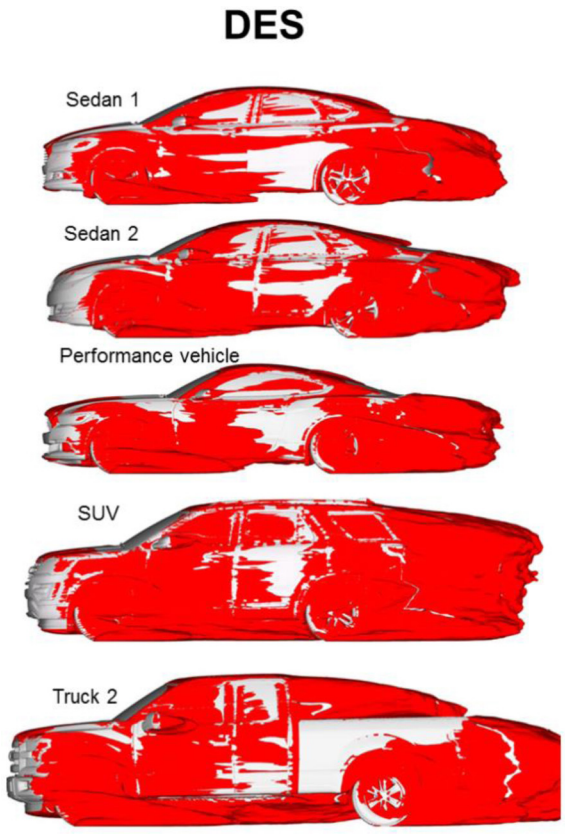


Figure 43. Isocontours of zero total pressure generated using the unsteady, DES turbulence model for moving ground cases.

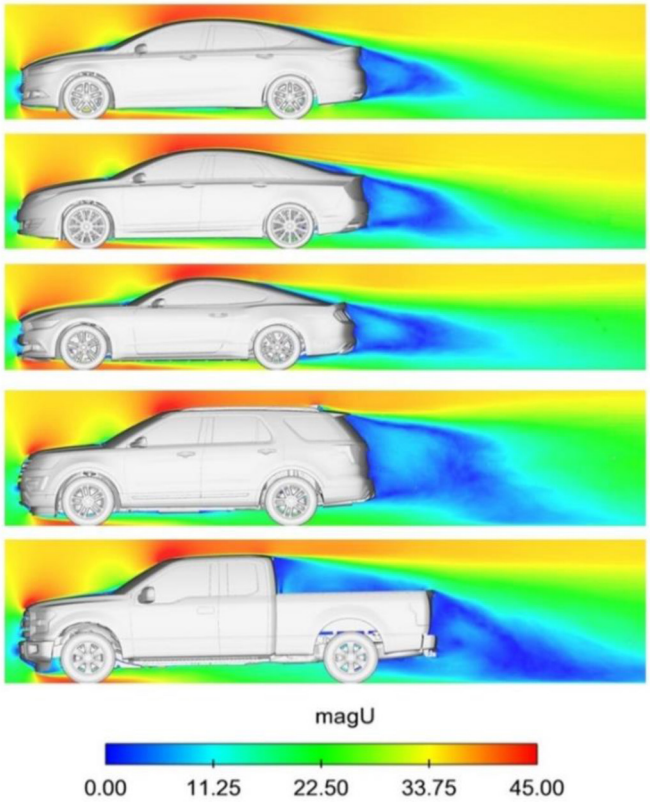


Figure 44. Contours of velocity magnitude generated using the unsteady, DES turbulence model for moving ground cases.

Summary and Conclusions

A combination of 54 different vehicle shapes and shape variants were evaluated against both static and moving ground wind tunnel experimental measurements. The ability of both transient DES and steady k–ω SST RANS simulations to correctly rank all 54 configurations was evaluated using the ranking accuracy metric. Both the DES and SST models achieved ranking accuracies greater than 90% overall, where DES showed an advantage of a few percentage points.

Transient simulation ranking accuracy of total vehicle C_d was found to be approximately equivalent to commercial transient lattice Boltzmann solver results even though a consistent upward bias in absolute C_d values was observed. This was true across the entire data set as well as within specific subsets of the data. Steady state ranking accuracy of total vehicle C_d was also found to be approximately equivalent to commercial transient lattice Boltzmann solver results. This was true across the entire data set as well as within specific subsets of the data.

C_d development plot comparisons confirmed that similar C_d development patterns were predicted by both steady state and transient simulations. The most significant variations were linked to flow structure differences between steady state and transient simulations observed in the tire wakes, underbody velocities and body wakes.

Analysis of specific subsets of the data set highlighted the fact that the ranking accuracy of transient simulations is slightly better than steady state across all subsets with the most significant improvement seen for trucks and SUVs.

The results of this study indicate that both steady state and transient simulations are capable of supporting general C_d trend analyses. Transient analyses are recommended for maximum trend accuracy, and in particular for truck and SUV models. However, the faster turnaround time for steady state simulations makes this a very time efficient option to support proportion studies and theme evaluations early in the design cycle when absolute accuracy is less critical.

The next steps for this study would include an investigation of the positive bias in absolute vehicle C_d, expansion of the validation set to expand the number of samples in each subset to investigate more subtle vehicle surface changes, and the addition of vehicle lift ranking accuracy as an evaluation metric.

References

1. OpenFOAM, v2.1.1, 2012. www.openfoam.com.
2. Lietz, R., Hupertz, B., Lewington, N., Silveira, R., , “Benchmarking of an Open Source CFD Process for Aerodynamics Prediction of Multiple Vehicle Types,” SAE Technical Paper 2011-01-0163.
3. Menter, F.R., 1994. Two-equation eddy-viscosity turbulence models for engineering applications. AIAA J. 32(8), 1598–1605.
4. Franke, J., Hellsten, A., Schlünzen, H., Carissimo, B., COST 2007. Best practice guideline for the CFD simulation of flows in the urban environment, Action 732, Quality assurance and improvement of micro-scale meteorological models.
5. Heft, A., Indinger, T., and Adams, N., "Introduction of a New Realistic Generic Car Model for Aerodynamic Investigations," SAE Technical Paper 2012-01-0168, 2012, doi:10.4271/2012-01-0168.

Contact Information

Robert Lietz
Vehicle Aerodynamics Technical Specialist and Core Supervisor
Ford Motor Company
rlietz@ford.com

Acknowledgments

The authors acknowledge support for this project from Burkhard Hupertz and Neil Lewington of Ford Motor Company.

Definitions and Abbreviations

CFD - Computational Fluid Dynamics

HPC - High Performance Computing

DES - Detached-Eddy Simulation

AGS - Active Grille Shutters

RANS - Reynolds Averaged Navier-Stokes

OPENFOAM® - Registered trademark of OpenCFD Limited, producer and distributor of the OpenFOAM software.

FVM - Finite Volume Method

LES - Large Eddy Simulation

The Engineering Meetings Board has approved this paper for publication. It has successfully completed SAE's peer review process under the supervision of the session organizer. The process requires a minimum of three (3) reviews by industry experts.

All rights reserved. No part of this publication may be reproduced, stored in a retrieval system, or transmitted, in any form or by any means, electronic, mechanical, photocopying, recording, or otherwise, without the prior written permission of SAE International.

Positions and opinions advanced in this paper are those of the author(s) and not necessarily those of SAE International. The author is solely responsible for the content of the paper.

ISSN 0148-7191

http://papers.sae.org/2017-01-1524